Atmos. Chem. Phys. Discuss., 12, 4941–4977, 2012
www.atmos-chem-phys-discuss.net/12/4941/2012/
doi:10.5194/acpd-12-4941-2012
© Author(s) 2012. CC Attribution 3.0 License.

Atmospheric Chemistry and Physics Discussions

This discussion paper is/has been under review for the journal Atmospheric Chemistry and Physics (ACP). Please refer to the corresponding final paper in ACP if available.

Strongly sheared stratocumulus convection: an observationally based large-eddy simulation study

S. Wang[1], **X. Zheng**[2], **and Q. Jiang**[1]

[1]Naval Research Laboratory, Monterey, CA, USA
[2]RSMA, University of Miami, Miami, FL, USA

Received: 2 February 2012 – Accepted: 5 February 2012 – Published: 13 February 2012

Correspondence to: S. Wang (wang@nrlmry.navy.mil)

Published by Copernicus Publications on behalf of the European Geosciences Union.

Abstract

Unusually large wind shears across the inversion in the stratocumulus-topped marine boundary layer (MBL) were frequently observed during VOCALS-REx. To investigate the impact of wind shear on the MBL turbulence structure, a large-eddy simulation (LES) model is used to simulate the strongly sheared MBL observed from Twin-Otter RF 18 on 13 November 2008. The LES simulated turbulence statistics agree in general with those derived from the measurements, with the MBL exhibiting a decoupled structure characterized by an enhanced entrainment and a turbulence intensity minimum just below the clouds. Sensitivity simulations show that the shear tends to reduce the dynamic stability of the inversion, enhance the entrainment mixing, and decrease the cloud water. Consequently, the turbulence intensity in the MBL is significantly weakened by the intense wind shear. The inversion thickens considerably and the MBL top separates from the cloud top, creating a finite cloud-free sublayer of 10–50 m thickness within the inversion, depending on the shear intensity. The wind shear enhances the turbulence buoyant consumption within the inversion, and simultaneously weakens the buoyant production in the cloud layer. These effects may result in different heating rates between the cloud and subcloud layer, leading to a process that tends to decouple the cloud from the subcloud layer. The decoupling process occurs even without solar radiation in the case of an intense wind shear similar to the observations.

1 Introduction

One of the most persistent features of the stratocumulus-topped MBL observed during VOCALS-REx (*V*ariability of the American Monsoons *O*cean-*C*loud-*A*tmosphere-*L*and *S*tudy-*R*egional *Ex*periment) is the unusually intense wind shear across the inversion. Averaged soundings along 20° S using aircraft measurements as well as rawindsondes launched from the R. H. Brown R/V clearly exhibit an approximate -4 to $-7\,\mathrm{m\,s^{-1}}$ and $4\,\mathrm{m\,s^{-1}}$ to $6\,\mathrm{m\,s^{-1}}$ jump across the inversion in the meridional and zonal wind

ACPD
12, 4941–4977, 2012

component, respectively (Bretherton et al., 2010; Wang et al., 2011; Zheng et al., 2011). The shear was frequently accompanied with a wind speed maximum just below the inversion. Unlike many other boundary layers where the shear is mainly a result of surface friction, the shear documented during VOCALS-REx is primarily caused by baroclinicity within the inversion, which is linked to the large-scale horizontal gradient of the inversion height (Bretherton et al., 2010; Wang et al., 2011). Perhaps for this reason, the wind shear tends to be unusually intense and persistent.

An example of the wind shear cases is presented in Fig. 1; the observations were taken during the Twin-Otter research flight 18 (RF18) near 72° W and 20° S on 13 November 2008. Two similar soundings taken at 12:08 UTC (07:08 LT) and 13:25 UTC (08:25 LT) are shown. The meridional wind components change sharply from $0\,m\,s^{-1}$ to $-9\,m\,s^{-1}$ across the inversion layer, whereas the zonal component changes only about $4\,m\,s^{-1}$. The wind variations within the boundary layer are significantly smaller than those across the inversion. The liquid water mixing ratio (q_c) reaches its maximum value ($\sim 0.3\,g\,kg^{-1}$) near the cloud top. A sharp temperature inversion caps the cloud layer with ~10 K jump; the associated moisture decrease is $\sim 2.5\,g\,kg^{-1}$.

Wind shear across the inversion is well known for its significant role in generating turbulent mixing and enhancing the entrainment rate in cloud-free convective boundary layers. For example, the shear is found to enhance the entrainment heat flux by producing Kelvin-Helmholtz wave like billows within the entrainment zone (Kim et al., 2003). The thickness of the layer is controlled by a balance among the shear generation, buoyancy consumption, and dissipation of turbulence kinetic energy (TKE) (Conzemius and Fedorovich, 2006). This balance is manifested by an equilibrium Richardson number of the layer that is close to the critical value 0.25 (Turner, 1973).

When the wind shear occurs at the stratocumulus cloud top, its effects are considerably more complex due to the interplay among the turbulent mixing, radiation and cloud water evaporation. The turbulent mixing driven by the wind shear may lead to local dissipation of clouds, as suggested by de Roode and Wang (2007) based on analysis of

ACPD
12, 4941–4977, 2012

turbulence data. A few model simulations, including large-eddy simulation (LES) studies, examine the overall turbulence and inversion characteristics in presence of wind shear. The reduction of cloud water due to the shear enhanced mixing may significantly decrease the longwave cooling rate near cloud top, leading to considerable weakening of the turbulence intensity (Chen and Cotton, 1987; Wang et al., 2008). Because of shear-enhanced mixing, a turbulent and unsaturated sublayer of several tens of meters may form just above clouds within the inversion (Moeng et al., 2005; Wang et al., 2008). The thickness of this sublayer can be further linked to the mean shear strength. (Wang et al., 2008). These broad features of the simulated shear mixing were confirmed by a few observational studies (e.g., Brost et al., 1982; Katzwinkel et al., 2011). After analyzing the high-resolution turbulence measurements within the inversion layer, Katzwinkel et al. (2011) suggests that presence of the turbulent and cloud-free layer may reduce the evaporation since moister and cooler air, relative to the non-turbulent air above the inversion, is entrained into clouds.

The research on turbulence dynamics of stratocumulus clouds has been generally focused on the interaction among the turbulence buoyant production, entrainment and turbulence structure (e.g., Lilly, 1968; Nicholls et al., 1984; Bretherton et al., 1997; Stevens, 2000). Roles of the shear have been rarely emphasized in the theories and analyses. Although the importance of the shear has been recognized in a few studies including those mentioned above, many questions remain unanswered. How does the shear affect the entrainment zone structure? Does it affect the entrainment? What is the impact of the shear on the decoupling process that tends to result in a layered MBL structure?

This study focuses on the observed case of the sheared stratocumulus convection presented in Fig. 1. LES model simulations and observations are used to address questions highlighted above. We will first provide descriptions of the LES model and simulation setups in Sect. 2 and discuss the overall turbulence structure, including evaluation of the model results using observations in Sect. 3. Further examination of the turbulent mixing in the entrainment zone and on the impact of the shear on

ACPD
12, 4941–4977, 2012

the decoupling process will be presented in Sects. 4 and 5, respectively. Section 6 summarizes the work.

2 LES model description and simulation setup

We use Naval Research Laboratory *C*oupled *O*cean/*A*tmosphere *M*esoscale *P*rediction *S*ystem-*L*arge-*E*ddy *S*imulation (COAMPS®-LES) model in this study (Golaz et al., 2005). Readers are referred to the paper for detailed description. Briefly, the anelastic approximation is assumed for efficient numerical computation; Deardorff's prognostic turbulence kinetic technique is used for the subgrid-scale model (Deardorff 1980); Bott positive definite advection scheme is applied to scalar advection (Bott, 1989); the four stream Fu-Liou radiation parameterization is used for both longwave and shortwave computation (Fu and Liou, 1992); a saturation adjustment scheme is used for the condensation and evaporation; and the precipitation processes are deactivated. At the top of the domain, a constant gradient condition is applied to all variables. The lateral boundary conditions are periodic. The model uses 281 × 281 grid points in horizontal with a uniform spacing $\Delta x = \Delta y = 25$ m. A vertically stretched grid (Δz) is designed to provide minimum grid spacing of 5 m within the inversion and gradually increased spacing to 25 m below and above the inversion. The grid system spans a volume of 7 km × 7 km × 2.3 km. The time step is 0.5 to 0.75 s. The choice of the resolution is, in part, based on our previous experience described in Wang et al. (2008) where a grid mesh of 10 m × 10 m × 5 m ($\Delta x \times \Delta y \times \Delta z$) produced a very similar turbulence structure to that of 30 m × 30 m × 5-to-20 m for a strongly sheared stratocumulus case. It is also consistent with the resolutions used for a number of LES case studies (e.g., Stevens et al., 2005; Golaz et al., 2005).

The surface turbulent fluxes in the simulations are specified using values calculated from the turbulence measurements made at the lowest level (~ 50 m) during RF18; they are listed in Table 1. Large-scale vertical motion changes linearly with the specified divergence below the boundary layer height and then remains at its z_i value for all

ACPD
12, 4941–4977, 2012

levels above. To keep the free atmospheric structure from departing significantly from the observation due to the subsidence and radiation, we applied a nudging term to all the variables above the inversion top with a time scale of 4 h. Simulation experiments showed that our results are not sensitive to the choice of this time scale.

Thermal wind is an essential aspect of the forcing as it defines magnitude of the wind shear for the simulations. We calculated daily averaged mean geostrophic winds for 13 November 2012 from COAMPS real-time forecast (Wang et al., 2011), which are plotted using a normalized MBL height in Fig. 2a. The meridional component (V_g) changes from 1 m s^{-1} below the inversion to −10 m s^{-1} just above it, which is consistent with the jump in the observed wind. The zonal component (U_g) changes significantly less across the inversion. These mesoscale model results clearly demonstrate that the observed wind shear is directly linked to the large-scale horizontal temperature gradient. Based on both the observations and the regional model results, we specify the geostrophic forcing as shown in Fig. 2b.

The initial conditions for $\bar{\theta}$ and $\bar{q_v}$ are specified according to the soundings at 12:08 UTC. Preliminary simulations indicate that an initially large wind shear leads to rapid cloud dissipation because the shear results in a peak in the turbulent mixing at the cloud top before a quasi-equilibrium between the turbulence and large-scale forcing is established. Therefore, we initialize the wind with constant profiles using values of (U_g, V_g) above MBL. Then the wind is nudged toward the geostrophic wind with a time scale of one hour. The nudging term is deactivated after the first hour of the simulation; the wind is then slowly adjusted toward the geostrophy while the turbulence gradually reaches equilibrium with the specified large-scale and surface conditions.

To evaluate the simulations against the observations, we perform three simulations with solar radiation processes included. Simulation SS (strong shear) corresponds to the observed strong shear case; simulation WS (weak shear) is designed to reduce the shear by one half; simulation NS (no shear) sets mean wind speed to zero. To isolate the shear impact, we also conduct another set of simulations in which the solar radiation is deactivated. The large-scale divergence and surface fluxes are specified

ACPD
12, 4941–4977, 2012

according to Table 1. All simulations start at 02:00 LT and end at 10:00 LT and are listed in Table 2 for reference.

3 Synopsis of turbulence structure

This section compares the overall turbulence structure among three simulations, i.e., SS, WS and NS, including evaluating the results using turbulence statistics computed from aircraft measurements. Because most of the measurements were made between 07:00 LT and 10:00 LT, all the LES profiles presented here are averaged between these two times with a sampling rate of 30 s. The LES time series are formed by taking averages every minute with this sampling rate. It should be noted that among all the LES runs, the large-scale conditions used in SS should best represent the observed MBL environment. Therefore, the evaluation with observations is mainly focused on the SS simulation.

As shown in Fig. 3, the simulated mean liquid water potential temperature ($\bar{\theta}_l$) and total water mixing ratio ($\bar{q}_t$) are very similar for all three simulations and comparable with the observations (Fig. 1a). Liquid water mixing ratio ($\bar{q}_c$) from SS is the smallest among three cases due to the strong wind shear; its maximum value is 2.6 g kg^{-1} compared with the observed q_c maximum of 3.1 g kg^{-1} shown in Fig. 1b. The SS simulated $\bar{v}$ has a -9.0 m s^{-1} jump across the inversion and reaches values close to zero near the surface, which is consistent with the observations. The simulated $\bar{u}$ is about 5 m s^{-1} in the mixed layer and then reduces to the value of geostrophic wind above the inversion, leading to a -3 m s^{-1} jump across the inversion. This appears to be inconsistent with the observations, which show a relatively small positive jump in Fig. 1. The inconsistency may be caused by an initial large geostrophic imbalance in $\bar{v}$, which contributed to a substantial acceleration of $\bar{u}$. The $\bar{u}$ shear, however, is significantly less than the $\bar{v}$ shear.

All three simulated $\overline{w'^2}$ profiles have a similar shape with a local minimum just below

ACPD
12, 4941–4977, 2012

the cloud base at 850 m, which in general is consistent with that derived from the observations as shown in Fig. 3d. The SS $\overline{w'^2}$, however, compares best with the observed with regard to both the shape and the magnitude, which are directly controlled by the buoyancy flux ($\rho_0 C_p \overline{w'\theta'_v}$) shown in Fig. 3e. All the simulated buoyancy fluxes compare favorably with the observations. In particular, the near zero values below the cloud base agree well with the corresponding minimum in the observation, which explains the local minimum values of $\overline{w'^2}$ just below the clouds. The decrease in positive $\rho_0 C_p \overline{w'\theta'_v}$ with increasing wind shear is the main reason why the overall magnitude of $\overline{w'^2}$ decreases from the case NS to SS. The large negative $\rho_0 C_p \overline{w'\theta'_v}$ in the inversion from SS reflects the effect of the shear enhanced mixing. Furthermore, the shear enhanced mixing reduces $\bar{q}_c$ in SS and WS (Fig. 3b), resulting in a considerable decrease in the radiative cooling compared with that in NS (Fig. 3f). This is a primary reason why the positive $\rho_0 C_p \overline{w'\theta'_v}$ decreases with increasing wind shear.

The turbulence intensity minimum just below clouds tends to result in different gradients of turbulent fluxes of conserved variables (e.g., q_t) between the cloud and subcloud layers. Consequently, the cloud layer evolves differently from the subcloud layer, leading toward a layered or decoupled MBL structure. This decoupling process plays an important role in the diurnal variation (Turton and Nicholls, 1987) and the stratocumulus-shallow cumulus regime transition (Bretherton et al., 1997).

The total momentum flux, defined by $\sqrt{\overline{w'u'}^2 + \overline{w'v'}^2}$, from the simulation SS agrees well with the observations with a maximum near the cloud top and a local minimum just below the cloud (Fig. 3g). Although the WS simulation has the correct shape of the momentum flux profile, its maximum value is significantly less than the observation. The large momentum flux near the MBL top reflects the effect of the wind shear, because the flux is directly linked to the shear. The minimum values below clouds are also related to the minimum in $\overline{w'^2}$ at those levels. Because the mean wind speed is close to zero in the case of NS, the simulated momentum flux does not resemble any

ACPD
12, 4941–4977, 2012

of the features exhibited in the observation.

Both the SS and WS simulated total water fluxes ($\rho_0 L\overline{w'q_t'}$) have the local minimum values near the cloud base and maximum near the cloud top, features consistent with the observation, although their magnitudes are larger (Fig. 3h). Once again, both the observed and shear-case simulated $\rho_0 L\overline{w'q_t'}$ clearly demonstrate the strong decoupling signature of drying in the upper and moistening in the lower portion of the MBL.

The third-moment of $w(\overline{w'^3})$, shown in Fig. 3i, is closely linked to the turbulence structure and organization. That is, the negative values imply that narrow and strong downdrafts dominate, whereas positive values suggest that updrafts are narrower and stronger. For NS, $\overline{w'^3}$ has a larger negative value than for WS and SS in the cloud layers, which is caused by the reduced radiative cooling rates in the shear cases (Nicholls, 1989). It may be also linked to the entrainment mixing generated evaporative cooling rates (Yamaguchi and Randall, 2012). This difference in $\overline{w'^3}$ can also be viewed in Fig. 4, which compares the w horizontal distribution among the cases at the levels of maximum buoyancy flux. For all three w fields, the downdrafts appear to be more intense and narrower than the updrafts, consistent with the negatively skewed w in cloud layers for all cases. The turbulence is clearly better organized by the downdrafts in the NS case relative to the two shear cases because both the downdrafts and updrafts are stronger and the cellular structure is better defined in the NS case. The strong shear case SS appears to have the least organized cellular structure.

To briefly summarize, the strong shear simulation (SS) compares best with the observations. Two main features emerge from both the observations and the LES results. First, there is a well-defined decoupled turbulence structure in terms of local minimum values below cloud base in all the second-moment turbulence statistics. Second, strong shear mixing near cloud top is indicated by a large momentum flux. Several key points can be drawn from the sensitivity simulations as follows: 1) The increased shear weakens the in-cloud turbulence intensity by reducing the cloud water, 2) the negative buoyancy flux at the cloud top is significantly augmented by the shear enhanced

ACPD
12, 4941–4977, 2012

mixing, and 3) the shear suppresses the cloud cellular structure.

4 Inversion layer

Because the wind shear occurs across the inversion, it directly impacts the dynamic stability of the inversion. This effect can have important implications on turbulence in this layer, and thus impacts the overall stratocumulus-topped MBL structure. This section focuses on the entrainment zone by comparing flow characteristics among different simulations.

We first compare the variances of θ_l, q_t, and q_c within the inversion in Fig. 5, which exhibits three fundamental features. First, the inversion layer thickness increases with wind shear intensity, ranging from 40 m for NS to 110 m for SS. Second, the cloud-top height, which can be diagnosed by the $\overline{q'^2_c}$ profiles, only changes by 20 m from the NS to SS runs. There clearly exists a finite cloud-free sublayer in the upper part of the inversion for each run. The sublayer thickness is the largest for SS and diminishes for NS. Third, even though the shear is the greatest for SS, its scalar variances are smaller than those for WS; it occurs because the gradients in the layer become weaker due to the significantly thickened inversion.

The gradient Richardson number is used to characterize the dynamic stability and to further examine the inversion structure. The Richardson number is defined as

$$Ri = \frac{g}{\bar{\theta}} \frac{\Delta\theta_{vl}/\Delta z}{\left(\frac{\Delta u}{\Delta z}\right)^2 + \left(\frac{\Delta v}{\Delta z}\right)^2} \quad (1)$$

where $\Delta(\ )$ denotes a vertical difference and $\theta_{vl} = \theta_l + 0.608 \cdot T \cdot q_t$. For our purpose, we compute the bulk Richardson number (Ri_b) across the thickness of the inversion layer. That is, $\Delta z_i = z_{itop} - z_{ibase}$, where z_{itop} is the level of the inversion layer top and z_{ibase} the level of the inversion layer base. All other vertical differences are also defined at these two levels. Because the vertical gradient of $\bar{\theta}_l$ increases significantly at the

ACPD
12, 4941–4977, 2012

inversion base and decreases at the top, z_{itop} can be defined as the level at which the second derivative of $\bar{\theta}_l$ is a local minimum, whereas z_{ibase} is the level at which it is a local maximum. We also calculate the cloud top height (z_{ctop}), which is defined as the level above which the cloud fraction falls below 0.5 %.

Figure 6 shows the temporal evolutions of z_{itop}, z_{ibase}, z_{ctop}, the mean wind shear (defined by $\left(\Delta\bar{u}/\Delta z\right)^2 + \left(\Delta\bar{v}/\Delta z\right)^2$), and Ri_b. The stair-stepped appearance of the curves is due to the fact that these heights are defined at the grid levels and no interpolation is performed. The strong shear in the SS case enhances turbulent mixing within the inversion and results in the highest z_{itop} and lowest z_{ibase}. Consequently, the thickness of the inversion layer ($\Delta z_i = z_{itop} - z_{ibase}$) reaches approximate 110 m at the end of the SS simulation compared to only 35 m for the WS and 20 m for the NS cases. A cloud-free sublayer is present in the upper inversion for all the simulations. But the sublayer from SS has the greatest thickness of about 60 m at the end of simulation; it is significantly larger than those from WS and NS, which are 25 m and 15 m, respectively.

The inversion layer thickness is controlled by the turbulent mixing. Smaller Ri_b tends to produce thicker Δz_i. This relationship can be clearly seen by comparing Δz_i and Ri_b from different cases. For example, Δz_i is 110 m with a value of Ri_b close to 0.33 for the SS case at the end of the simulation, while Δz_i is 35 m with the Ri_b close to 0.5 in terms of the WS case. It is notable that Ri_b of SS stays slightly above 0.3 for last 3 h, despite the increase of Δz_i from 52 m to 110 m. In fact, there are very small jumps in Ri_b from time to time corresponding to the increases in Δz_i and decrease in the wind shear as indicated by small arrows in Fig. 6e. Between these jumps, Ri_b of SS gradually decreases due to an increase in the shear (Fig. 6d). Therefore, for SS, Ri_b no longer decreases even though the shear tends to intensify. Instead, the inversion layer thickens to reduce the wind shear and to maintain an equilibrium Ri_b, which is approximate 0.3 for this case. The phenomenon that an equilibrium bulk Richardson number can be reached with the increasing wind shear have been studied by a number of authors as discussed in the introduction section. For stratocumulus cloud conditions, similar results were also found in a LES study using a strong wind shear case along the

ACPD
12, 4941–4977, 2012

central coast of California by Wang et al. (2008). These results suggest that there exists a feedback mechanism between the large-scale conditions and turbulence dynamics in controlling the inversion stability. The large-scale subsidence and radiative cooling near the cloud top tends to create a sharp inversion with a strong dynamic stability, whereas the wind shear acts to destabilize the inversion. When the shear is sufficiently intense such that Ri_b approaches the critical value (0.25), any further increase in the shear is likely to result in enhanced mixing which substantially deepens the inversion layer. Consequently, the wind shear is reduced and Ri_b adjusts back to a larger value. Eventually, an equilibrium value is reached. Through this process, the MBL height increases with a deeper inversion layer.

Links between the flow structure and the shear are explored further using an instantaneous local Richardson number (Ri) based on the values at adjacent grids without any averaging in Eq. (1). Probability density functions (PDFs) of Ri are calculated at three levels within the cloud-free sublayers identified by the cloud fraction and $\bar{\theta}_l$ profiles. The PDFs are shown in Fig. 7. In experiment SS, the PDF peaks near an Ri value of 0.25 with a narrow distribution, whereas for WS it peaks near the Ri of 0.85 with a significantly broader distribution. If the flow with Ri less than 0.25 is considered fully turbulent and for Ri between 0.25 and 1 classified as intermittently turbulent, we can estimate the fractional coverage of the potentially turbulent flows based on the Ri. The fraction of fully turbulent flow for SS, WS and NS is 0.3, 0.002, and 0; the fraction for intermittently turbulence is 0.66, 0.63, and 0.5×10^{-3}, respectively. This means that 96 % of the flow is either turbulent or intermittently turbulent for SS. This ratio is about 63 % for WS and nearly zero for NS. The turbulence activity is considerably more intense with the stronger wind shear.

To further examine the relationship between turbulence and Ri, we show the joint PDF of Ri with w', θ_v' and q_v' at the levels within the cloud-free sublayers in Fig. 8. Large flow variability for all the variables occurs near 0.25 of Ri for SS, 0.8 for WS because the PDFs of Ri are maximized at these values (Fig. 7a). The variability for SS is significantly larger than that for WS due to the local environment, which is dynamically

ACPD
12, 4941–4977, 2012

less stable for the former than for the latter. It is also interesting to note that the negative q_v' and positive θ_v' are more associated with larger Ri. These fluctuations are likely strongly influenced by the entrained air; their variability is suppressed by the stronger dynamic stability. Because Ri for NS is very large, with a mean of ~ 200, and a broad distribution, the scatter plots are shown only for the lower end of Ri. In general, no systemic turbulence is present at this level for the NS case.

The wind shear reduces the dynamical stability of the inversion in a thermodynamically very stable environment. This reduction may enhance turbulent mixing within the inversion layer, leading to an increase in its thickness and creating a finite turbulent and cloud-free sublayer separating the MBL top and the cloud top. These LES results in general agree with the detailed observation analysis by Katzwinkel et al. (2011). Their analysis shows that the inversion layer is turbulent with the gradient Ri ranging between 0.2 to 0.7 in the inversion layer and the depth of the cloud-free sublayer between 37 m and 85 m.

5 Entrainment rate and decoupling

An important common feature of the above simulations is the decoupled turbulence structure as shown in Fig. 3; that is, a minimum is present just below clouds in each of the three turbulent fluxes (i.e. $\overline{w'^2}$, $\rho_0 L\overline{w'q_t'}$, $\rho_0 C_p\overline{w'\theta_v'}$). What causes the decoupling? It is well known that the cloud solar absorption tends to stabilize the MBL and decouple the cloud from the subcloud layer (Nicholls, 1984). Another possible contributing factor is the wind shear, because it enhances the entrainment mixing as characterized by the large negative buoyancy flux (Fig. 3e). All these simulations, however, include solar radiation, making it difficult to evaluate the shear impact on the decoupling. To isolate the shear effect, we perform three additional simulations, SSN, WSN, and NSN, which exclude the solar radiation and use the same shear conditions as those in the first set of three cases (SS, WS and NS).

Before proceeding to analyze the decoupling, we provide more evidence from the

ACPD
12, 4941–4977, 2012

simulations that the shear indeed enhances the entrainment. For this purpose, the entrainment velocity, w_e, is calculated from

$$w_e = \frac{d z_{itop}}{d t} + D \cdot z_{itop} \quad (2)$$

where D is the large-scale divergence listed in Table 1. The computed w_e together with Ri_b and the inversion thickness (Δz_i) are summarized in Table 2.

The inversion layer thickness (Δz_i) increases with the shear intensity and the no-shear cases (i.e., NS and NSN) have the minimum values among the simulations. The minimum Ri_b is reached in the SS simulation where there is a strong shear as well as a slightly weakened temperature gradient due to the solar absorption warming in the cloud layer. There is a general trend of high Δz_i being correlated with low values of Ri_b, although the relationship is not monotonic. The entrainment rate w_e increases with decreasing Ri_b for both the solar simulations (SS, WS and NS) and no-solar simulations (SSN, WSN, NSN). The maximum w_e is obtained in the SSN case in which the shear is the strongest. This further confirms the previous assertion that the entrainment mixing is enhanced by the wind shear in these simulations.

The shear-enhanced entrainment considerably affects the turbulence structure as shown in Fig. 9. The maximum buoyancy flux ($\rho_0 C_p \overline{w'\theta'_v}$) is consistently weakened with increasing shear. The larger the shear is, the smaller the in-cloud buoyancy flux is. The minimum just below clouds decreases in this weakening process and approaches zero in the SSN case. This is a departure from the previous cases (i.e., SS, WS or NS) for which the $\rho_0 C_p \overline{w'\theta'_v}$ profiles are quite similar (Fig. 3f), suggesting that the solar warming has in part concealed the shear effect in the cloud layer. Being consistent with the $\rho_0 C_p \overline{w'\theta'_v}$ profiles, $\overline{w'^2}$ is reduced considerably with intensifying shear. It obtains a local minimum just below the cloud base for the strongest shear case (SSN). This minimum in $\overline{w'^2}$ leads to a non-linear total water flux ($\rho_0 L \overline{w'q'_t}$) profile, resulting in a larger drying tendency for the cloud layer than for the subcloud layer. Although the $\rho_0 L \overline{w'q'_t}$ profile from either WSN or NSN is clearly linear, the former has a larger drying

ACPD
12, 4941–4977, 2012

tendency than the latter, as shown in Fig. 9c, indicative of enhanced entrainment for WSN.

The shear mixing also affects the MBL heat budget represented by the heat ($\rho_0 C_p \overline{w'\theta_l'}$) and radiative fluxes shown in Fig. 9d,e. The magnitude of the entrainment heat flux substantially increases due to the shear-enhanced mixing, whereas the in-cloud heat flux decreases due to the reduced radiative cooling – this reduction is also clearly seen in Fig. 3f. In general, with increasing wind shear, the entrainment warming increases and eventually dominates the radiative cooling. To quantify this change in the heat budget, we calculate the ratio of the entrainment warming to the total radiative cooling in the MBL, i.e., $\Delta F_\theta / \Delta F_R$, where Δ denotes the difference between the most negative buoyancy level and the surface. This ratio was used by Stevens et al. (2005) to evaluate the decoupling process and the values calculated from our simulations are listed in Table 2. It is seen that the ratio obtains the maximum value (1.2) for SSN and the smallest for NSN (0.6). A value larger than one implies that the entrainment warming is greater than the radiative cooling, suggesting that the decoupling is likely to occur. The maximum ratio for SSN (1.2) is close to, but below the critical value (1.35) for decoupling proposed by Stevens et al. (2005). For NSN, the radiative cooling is clearly the dominant driving force since the ratio is only 0.6. The other two weak shear cases (WSN and FSN) have significant entrainment warming, although the ratio does not go above one.

The decoupling process in the strong shear case (SSN) should also be reflected in the mean temperature and moisture profiles. As shown in Fig. 10, the MBL becomes warmer and drier with increasing wind shear. More importantly, the gradients of both $\bar{\theta}_l$ and $\bar{q}_t$ at the cloud base for SSN develop and become distinctively different from other cases. This further confirms that the cloud layer becomes partially decoupled from the subcloud layer for this case, even though the degree of decoupling appears to be weak since no significant decrease in the total cloudiness is found.

The skewness of w gives a dimensionless measure of asymmetry of the PDF. Figure 9f shows that there is no significant difference in the skewness in the cloud layer

ACPD
12, 4941–4977, 2012

between the shear and shear-free cases even though $\overline{w'^3}$ increases with the shear (not shown here but can be inferred from Fig. 3f). Consequently, the reduced $\overline{w'^3}$ for the shear cases is mainly due to a weaker turbulence intensity, i.e., $\overline{w'^2}$, instead of the asymmetry of the distribution.

One important feature of the shear effect is a simultaneous increase in the TKE buoyant consumption near the inversion, and decrease in the buoyant production in the cloud layer. This feature significantly contributes to the decoupling process, because both the intense entrainment warming and weak in-cloud turbulence tend to accumulate heat in the cloud layer, leading to different heating rates between the cloud and the subcloud layer. A useful parameter for quantifying this feature is the ratio of the integrated buoyant consumption to the production, defined as

$$A = \frac{-\int_0^{z_{\mathrm{itop}}} \overline{w'\theta'_v}(<0)\,dz}{\int_0^{z_{\mathrm{itop}}} \overline{w'\theta'_v}(>0)\,dz}. \quad (3)$$

This ratio is used in mixed-layer models for parameterization of stratocumulus clouds (e.g., Randall 1984). The larger the ratio A becomes, the more dominant the entrainment warming is and the more likely decoupling occurs. As shown in Table 2, the ratio A is 0.39 for SSN which is much larger than 0.014 for NSN. This suggests that the turbulence is not strong enough (i.e., the weak buoyant production) to redistribute the overwhelming entrainment warming (i.e., the large buoyant consumption) in the SSN case. The weak shear cases produce the A values that are between 0.034 and 0.14, markedly smaller than that of the strong shear cases. It implies that the strong turbulence can efficiently redistribute the entrained warm air such that a well-mixed layer is maintained. Another version of the ratio A, focused on the buoyant consumption in the subcloud layer, is developed with mixed-layer models by Turton and Nicholls (1987) and Bretherton et al. (1997) (also see Stevens, 2000). They argue that the ratio needs

ACPD
12, 4941–4977, 2012

to be in the range of 0.15–0.4 for decoupling to occur. The result presented here is different from theirs as the strong shear case (SSN) does not clearly show negative buoyancy flux in the subcloud layer.

So far, all the shears included in the simulations are driven by the large-scale baroclinicity associated with the sloping MBL. Another common mechanism of wind shears is surface friction under a barotropic boundary layer condition. These two types of wind shear should have similar dynamic effects on the MBL as they exert a similar control on the inversion layer stability. To confirm this hypothesis, we further perform another simulation with a wind shear driven by the surface friction. Since the observed surface stress is small due to weak surface winds, we intentionally increase the observed stress by a factor of 5 to produce a noticeable wind shear across the inversion. This simulation is designated as FCN and listed in Table 2. The final wind shear intensity for this case is $\Delta\bar{u} \sim -2\,\mathrm{ms}^{-1}$ and $\Delta\bar{v} \sim 3.5\,\mathrm{ms}^{-1}$, a slightly weaker than that in the WS case. Figures 9–10 show that the turbulence profiles of FSN stay between those of SSN and NSN, exhibiting weaker turbulence intensity and buoyancy forcing, and a larger moisture flux in the cloud layer than those of NSN.

The shear-enhanced entrainment mixing inevitably impacts the buoyantly driven convective circulation within stratocumulus clouds, since it reduces the turbulence buoyant production. To examine the effect, we conditionally sample the data from the no-solar simulations using one standard deviation of w (σ_w) to select convective updraft or downdraft grid points. That is, a grid point is defined as part of updrafts (or downdrafts) if $w \geq \sigma_w$ (or $w \leq -\sigma_w$). We then calculate averaged perturbations for variables of updrafts and downdrafts; they are defined as the averaged up-downdraft variables minus the ensemble means (e.g., $\theta'_{vu} = \theta_{vu} - \bar{\theta}_v$, where the subscript u denotes a updraft-averaged variable).

The buoyancy and vertical motion perturbations along with the corresponding standard deviations are shown in Fig. 11 to assess the change in the circulation due to wind shear. The buoyancy perturbations in updrafts (θ'_{vu}) and downdrafts (θ'_{vd}) in clouds are consistently reduced with increasing wind shear. For SSN, both θ'_{vu} and θ'_{vd} are nearly

ACPD
12, 4941–4977, 2012

zero just below clouds, compared with the larger magnitudes (∼ 0.04 K and 0.02 K) for NSN and WSN. Near cloud tops, driven by radiative cooling, θ'_{vu} and θ'_{vd} of SSN obtain their local maximum (∼ 0.04 K) that is smaller than that of NSN (0.07 K) and WSN (0.05 K). A weakened convective circulation is clearly indicated by the slowed updraft (w'_u) and downdraft (w'_d) motions. Magnitudes of these perturbations are consistent with the variability measured by the standard deviations. The largest difference in σ_{θ_v} among the simulations occurs just below the cloud base where its values for SSN and WSN are smaller than those of NSN. The σ_w magnitude decreases with increasing wind shear among these cases. The difference is more notable in the subcloud layer. The impacts on the convective circulation are mainly driven by the different radiative cooling rates since it is the main driving force for the convection as discussed by Nicholls (1989).

Based on the above analyses, it can be concluded that the intense wind shear across the inversion indeed causes the cloud layer being weakly decoupled from the subcloud layer for the SSN simulation. Even though the shear does not lead to decoupling for the WSN (or FSN) case, it nevertheless enhances the entrainment. The enhanced mixing increases the negative buoyancy flux which dominates the radiative cooling in SSN. In both the weak and strong shear cases (WSN and SSN), positive buoyancy flux within and just below the clouds decrease markedly compared to that of the shear-free case (NSN). This occurs mainly because the shear mixing near the cloud top reduces the cloud water, leading to a reduction in the radiative cooling. The enhanced entrainment also introduces more buoyant air to clouds so that the buoyancy flux is further reduced below clouds. Combination of the enhanced entrainment warming and reduction in the radiative cooling leads to the decoupling process.

It should be emphasized that the impact of the shear on the entrainment may depend on the characteristics of the inversion. A weaker inversion with a strong wind shear may result in a decrease in the entrainment rate as result of significantly weakened radiative cooling as shown in Wang et al. (2008). Katzwinkel et al. (2011) argued that w_e should scale with the depth of the turbulent and cloud-free sublayer; thus it may decrease with

ACPD
12, 4941–4977, 2012

an increase in the sublayer thickness caused by the enhanced shear. Although our study is not comprehensive enough to address these issues, more detailed numerical modeling and observational studies are clearly needed to provide new insights in the entrainment mixing process under strong wind shear conditions.

6 Summary

Wind shear always exists across the inversion in the stratocumulus-topped MBL, either due to surface friction or baroclinicity associated with the sloping MBL. Despite the difference in their origins, both types of wind shear strongly control the dynamic stability of the inversion layer, which can be measured by the gradient Richardson number. Therefore, the wind shear may significantly affect the cloud-top entrainment, as well as the turbulence structure of stratocumulus convection. While the importance of wind shear is well recognized, there have been only a few focused studies on sheared stratocumulus convection. In this study, we examine the impact of the wind shear on the turbulence structure using LES simulations and sensitivity experiments based on observations from the Twin-Otter RF18 during VOCALS-REx.

Two sets of simulations have been performed. The first experiment set uses different wind shear intensities (i.e., strong shear (SS), weak shear (WS) and no shear (NS)) and includes solar radiation calculation for comparison with the observations. The wind shear intensity is regulated by the vertical gradient of the geostrophic wind across the inversion that represents part of the large-scale forcing. To isolate the shear effect from that of cloud solar absorption, a second set of simulations is performed; they exclude the solar radiation calculation, but have the same shear conditions (i.e. SSN, WSN, and NSN in Table 2). An additional simulation (FSN) is also performed to assess the wind shear forced by the surface friction under barotropic conditions.

Our results show a reasonable agreement between the observations and the shear simulations with solar radiation. In particular, the SS simulation compares the best with observations in terms of the turbulence statistics profiles. Decoupling is clearly

ACPD
12, 4941–4977, 2012

seen in both the observed and modeled turbulence structures characterized by a local minimum below clouds for the fluxes such as $\overline{w'^2}$, $\rho_0 L\overline{w'q_t'}$, and $\rho_0 C_p\overline{w'\theta_v'}$ for these cases The shear-enhanced mixing is also indicated by similarly large momentum fluxes near the cloud top for both the SS simulation and observations.

The increased shear reduces the bulk Richardson number (Ri_b) of the inversion layer, enhances the mixing, and therefore thickens the inversion layer. The Ri_b appears to have a lower bound at ~ 0.3. Further increasing the wind shear does not lead to an additional reduction of Ri_b, rather, the inversion layer thickness increases such that Ri_b adjusts back toward 0.3. This suggests that the dynamic stability of the inversion is controlled by the interplay among the various large-scale and turbulent mixing processes. The role of the shear is to generate turbulence by destabilizing the inversion layer, whereas the turbulent mixing feeds back to ensure that a dynamically stable inversion is maintained. This is consistent with a number of previous observations and numerical simulations , which found an equilibrium bulk Richardson number is reached after large wind shear is applied (e.g., Turner, 1973; Conzemius and Fedorovich, 2006; Wang et al., 2008).

The shear-enhanced mixing leads to a clear separation of the MBL top (where turbulence diminishes) from the cloud top (where cloud fraction goes to zero), creating a finite cloud-free sublayer in the upper inversion. This sublayer thickness increases with increasing wind shear and decreasing Ri_b. These results are, in general, consistent with recent observational studies by Katzwinkel et al. (2011). Using the local Ri in the sublayer, we estimate that 96 % of the flow is either turbulent or intermittently turbulent for the strong shear case (SS); this fraction is about 63 % for weak shear case (WS) and 0 for the shear-free case (NS). The turbulence activity increases considerably with increasing wind shear. For the shear-free condition, this sublayer is thin and the turbulence activity is very weak.

The wind shear enhances the TKE buoyant consumption within the inversion, whereas it weakens the buoyant production in the cloud layer. Both effects tend to stabilize the stratocumulus-topped MBL. Our no-solar simulations show that the intense

ACPD
12, 4941–4977, 2012

wind shear (SSN) alone can lead to a decoupling process in which the minimum buoyancy flux in sub-cloud layer is close to zero and nonlinearity in the total water flux develops. In the weak shear case (WSN) where no decoupling occurs, a decrease in the buoyancy flux in the sub-cloud layer and increase in the entrainment flux is apparent, indicative of an overall weakening of the buoyancy forcing owing to wind shear. The entrainment rate is shown to increase in general with the shear intensity. Because of the change in the turbulence buoyant production, the convective circulation is also impacted by the enhanced shear mixing. Overall, the convection becomes weaker owing to the reduced buoyancy forcing. Specifically, the buoyancy forcing for the convective up-down drafts in the subcloud layer is close to zero.

Results of this study also highlight that the wind shear impacts the turbulence structure of the MBL by directly changing the dynamic stability of the inversion, which is critical for the determination of the entrainment mixing. Therefore, the bulk Richardson number defined by Eq. (1), as a measure of the inversion dynamic stability, should be considered as a key control parameter in parameterizations of the entrainment rate. Most of previous parameterizations use integrated buoyancy flux without including wind shear in the definition of bulk Richardson number (e.g., Grenier and Bretherton, 2000). We believe that a bulk Richardson number based on a combination of wind shear and integrated buoyancy flux represents more accurately the dynamic stability of the inversion in entrainment parameterizations. This type of parameterization already has been developed for a sheared cloud-free convective boundary layer (e.g., Conzemius and Fedorovich, 2007).

Because wind shear controls the dynamic stability of the inversion, it may contribute to the decoupling process that plays a major role in the transition from overcast stratocumulus to scattered shallow cumulus clouds. Given same large-scale conditions such as the lower tropospheric stability and sea surface temperature, a stronger wind shear across the inversion may be more favorable for the decoupling process to occur. Therefore, the shear effects on the decoupling and the cloud regime transition processes should be considered and further studied. These effects may be particularly

ACPD
12, 4941–4977, 2012

important for the stratocumulus-topped MBL in the southeast Pacific where the wind shear is persistent and relatively intense.

Acknowledgement. We thank James Doyle for his valuable review of an early draft. Shouping Wang benefitted from many in-depth discussions with Qing Wang on wind shears over the years. We are also very grateful to the Twin Otter staff and crew for the unique and high quality dataset. This work was supported by the Office of Naval Research (ONR) under Program Element (PE) 0602435N. COAMPS® is a registered trademark of the Naval Research Laboratory.

References

Bott, S.: A positive definite advection scheme obtained by nonlinear renormalization of the advective fluxes, J. Atmos. Sci., 117, 1006–1015, 1989.

Bretherton, C. S. and Wyant M. C.: Moisture transport, lower-tropospheric stability, and decoupling of cloud-topped boundary layers, J. Atmos. Sci., 54, 148–167, 1997.

Bretherton, C. S., Wood, R., George, R. C., Leon, D., Allen, G., and Zheng, X.: Southeast Pacific stratocumulus clouds, precipitation and boundary layer structure sampled along 20° S during VOCALS-REx, Atmos. Chem. Phys., 10, 10639–10654, doi:10.5194/acp-10-10639-2010, 2010.

Brost, R. A., Wyngaard, J. C., and Lenschow D. H.: Marine stratocumulus layers. Part II: Turbulence budgets, J. Atmos. Sci., 39, 818–836, 1982.

Chen, C. and Cotton, W. R.: The physics of the marine stratocumulus-capped mixed layer, J. Atmos. Sci., 44, 2940–2950, 1987.

Conzemius, R. J. and Fedorovich, E.: Dynamics of sheared convective boundary layer entrainment. Part I: Methodological background and large-eddy simulations, J. Atmos. Sci., 63, 1151–1178, 2006.

Conzemius, R. J. and Fedorovich, E.: Bulk models of the shear convective boundary layer: evaluation through large eddy simulations, J. Atmos. Sci., 64, 786–807, 2007.

De Roode, R. S. and Wang, Q.: Do stratocumulus clouds detrain? FIRE I data revisited, Bound.-Lay. Meteorol., 122, 479–491, 2007.

Deardorff, J. W.: Stratocumulus-capped mixed layers derived from a three dimensional model, Bound.-Lay. Meteorol., 18, 495–527, 1980.

ACPD

12, 4941–4977, 2012

Fu, Q. and Liou, K.-H.: On the correlated k-distribution method for radiative transfer in nonhomogenous atmospheres, J. Atmos. Sci., 49, 2139–2156, 1992.

Golaz, J.-C., Wang, S., Doyle, J. D., and Schmidt, J. M.: COAMPS™ LES: model evaluation and analysis of second and third moment vertical velocity budgets, Bound.-Lay. Meteorol., 116, 487–517, 2005.

Grenier, H. and Bretherton, C. S.: A moist PBL parameterization for large-scale models and its application to subtropical cloud-topped marine boundary layers, Mon. Weather Rev., 129, 357–377, 2011.

Katzwinkel, J., Siebert, H., and Shaw, R. A.: Observation of a self-limiting, shear-induced turbulent inversion layer above marine stratocumulus, Bound.-Lay. Meteorol., doi:10.1007/s10546-011-9683-4, 2011.

Lilly, D. K.: Models of cloud-topped mixed layers under a strong inversion, Q. J. Roy. Meteor. Soc., 94, 292–308, 1968.

Moeng, C.-H., Stevens, B., and Sullivan, P. P.: Where is the interface of stratocumulus-topped PBL? J. Atmos. Sci., 62, 2626–2631, 2005.

Nicholls, S.: The dynamics of stratocumulus: aircraft observations and comparisons with a mixed-layer model, Q. J. Roy. Meteor. Soc., 110, 784–820, 1984.

Nicholls, S.: The structure of radiatively driven convection in stratocumulus, Q. J. Roy. Meteor. Soc., 115, 487–511, 1989.

Randall, D. A.: Buoyant production and consumption of turbulent kinetic energy in cloud-topped mixed layer, J. Atmos. Sci., 41, 402–413, 1984.

Stevens, B.: Cloud transitions and decoupling in shear-free stratocumulus-topped boundary layers, Geophys. Res. Lett., 27, 16, 2557–2560, doi:10.1029/1999GL011257, 2000.

Stevens, B., Moeng, C.-H., Ackerman, A. S., Bretherton, C. S., Chlond, A., de Roode, S., Edwards, J., Golaz, J.-C., Jiang, H., Khairoutdinov, M., Kirkpatrick, M. P., Lewellen, D. C., Lock, A., Müller, F., Stevens, D. E., Whelan, E., and Zhu, P.: Evaluation of large-eddy simulations via observations of nocturnal marine stratocumulus, J. Atmos. Sci., 133, 1443–1461, 2005.

Turner, J. S.: Buoyancy Effects in Fluids, Cambridge University Press, 368 pp., 1973.

Turton, J. D. and Nicholls, S.: A study of the diurnal variation of stratocumulus using a multiple mixed layer model, Q. J. Roy. Meteor. Soc., 113, 969–1009, 1987.

Yamaguchi, R. and Randall, D. A.: Cooling of entrained parcels in a large-eddy simulation, J. Atmos. Sci., in press, 2012.

Wang, S., Golaz, J.-C., and Wang, Q.: Effect of intense wind shear across the inversion on

ACPD
12, 4941–4977, 2012

stratocumulus clouds, Geophys. Res. Lett., 35, L15814, doi:10.1029/2008GL033865, 2008.
Wang, S., O'Neill, L. W., Jiang, Q., de Szoeke, S. P., Hong, X., Jin, H., Thompson, W. T., and Zheng, X.: A regional real-time forecast of marine boundary layers during VOCALS-REx, Atmos. Chem. Phys., 11, 421–437, doi:10.5194/acp-11-421-2011, 2011.
Zheng, X., Albrecht, B., Jonsson, H. H., Khelif, D., Feingold, G., Minnis, P., Ayers, K., Chuang, P., Donaher, S., Rossiter, D., Ghate, V., Ruiz-Plancarte, J., and Sun-Mack, S.: Observations of the boundary layer, cloud, and aerosol variability in the southeast Pacific near-coastal marine stratocumulus during VOCALS-REx, Atmos. Chem. Phys., 11, 9943–9959, doi:10.5194/acp-11-9943-2011, 2011.

ACPD
12, 4941–4977, 2012

Table 1. Large-scale and surface conditions.

Surface stress ($N\,m^{-2}$)	Latent heat flux ($W\,m^{-2}$)	Sensible heat flux ($W\,m^{-2}$)	Divergence (s^{-1})	Surface pressure (hPa)	Simulation hours (LT)
0.014	30.4	7.2	4.0×10^{-6}	1013.6	02:00–10:00

ACPD
12, 4941–4977, 2012

Table 2. Simulation conditions and results based on last 3 h averages.

Runs	Shear Condition	Large-scale/ Sfc conditions	Solar radiation	Δz_i (m)	Ri_b	w_e (mm s^{-1})	$-\Delta F_\theta/\Delta F_R$	A
SS	Strong (obs)/ Baroclinic	Table 1	Yes	92	0.34	5.4	na	0.38
WS	Weak/ Baroclinic	Table 1	Yes	35	0.61	2.5	na	0.14
NS	No mean wind	Table 1	Yes	26	na	1.8	na	0.066
SSN	Same as SS	Table 1	No	90	0.37	7.6	1.2	0.39
WSN	Same as WS	Table 1	No	37	0.71	5.5	0.9	0.060
NSN	Same as NS	Table 1	No	27	na	3.9	0.6	0.014
FSN	Weak/ $V_g = 8\,\mathrm{m\,s^{-1}}$, $U_g = 0.0$	Table 1 except stress = 0.07 N m^{-2}	No	35	1.16	4.6	0.8	0.034

ACPD
12, 4941–4977, 2012

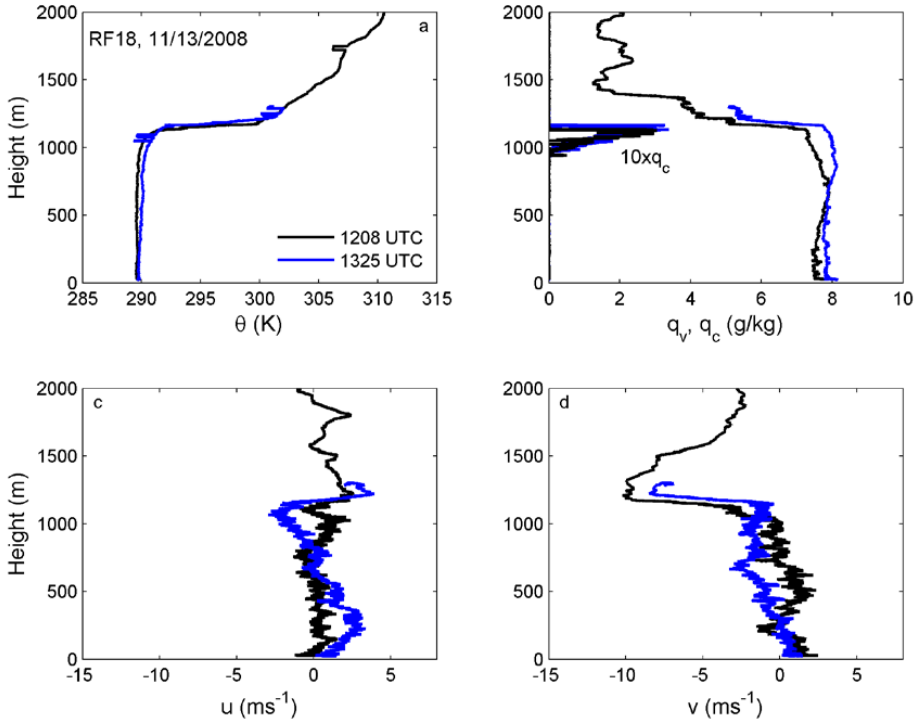

Fig. 1. Two soundings taken near 72° W and 20° S during RF18 of Twin-Otter, 13 November 2008.

ACPD
12, 4941–4977, 2012

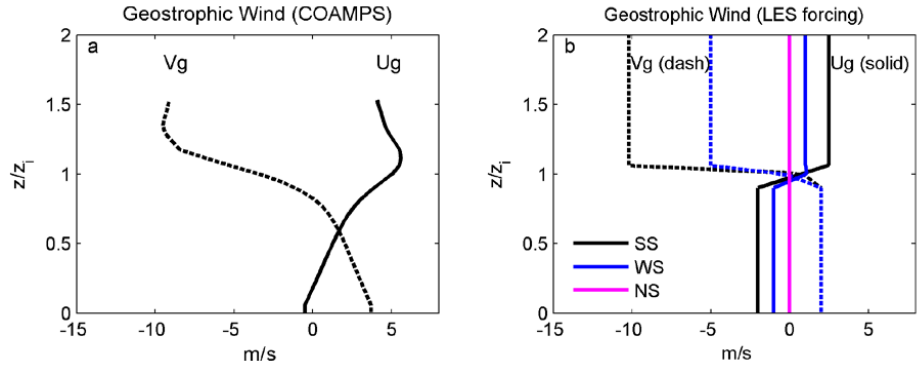

Fig. 2. Specification of geostrophic wind for LES simulations. **(a)**: daily averaged geostrophic winds on 13 November 2008, derived from the COAMPS regional forecast (Wang et al., 2010); and **(b)**: specified geostrophic winds for simulations. Dashed lines denote meridional components, solid zonal components.

ACPD
12, 4941–4977, 2012

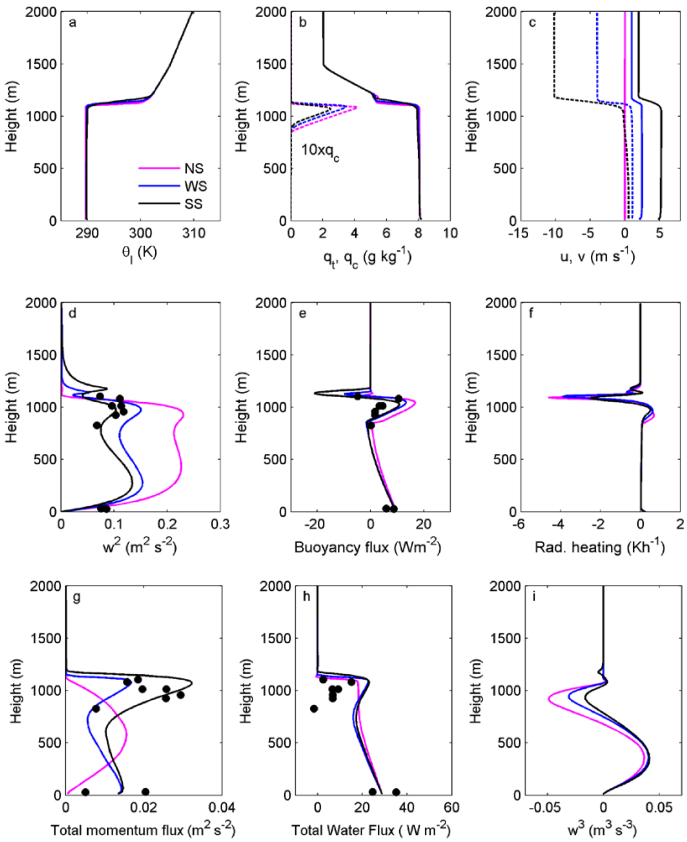

Fig. 3. Simulated mean and turbulence variables. Solid or dashed lines denote the simulated results; black dots are derived from the measurements. **(a)** $\bar{\theta}_l$; **(b)** $\bar{q}_t$ or $\bar{q}_c$; **(c)** $\bar{u}$ (solid) and $\bar{v}$ (dashed); **(d)** $\overline{w'^2}$; **(e)** $C_p\rho_0\overline{w'\theta'_v}$; **(f)** Radiative heating; **(g)** total momentum flux; **(h)** $L\rho_0\overline{w'q'_t}$; **(i)** $\overline{w'^3}$.

ACPD
12, 4941–4977, 2012

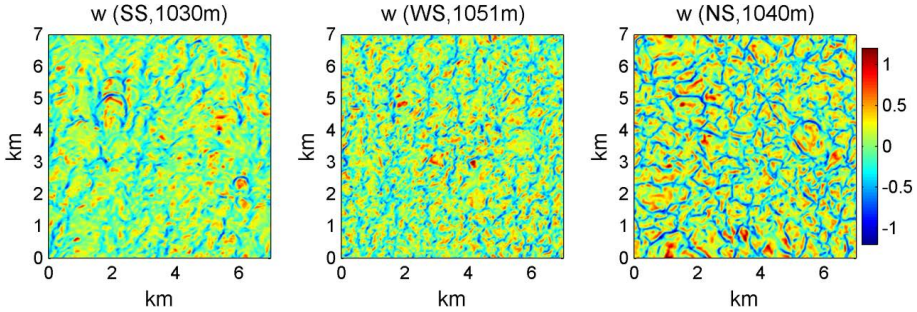

Fig. 4. Plan view of w' at the maximum buoyancy level at 09:00 LT for each simulation. Left panel is for SS, center WS, and right NS.

ACPD
12, 4941–4977, 2012

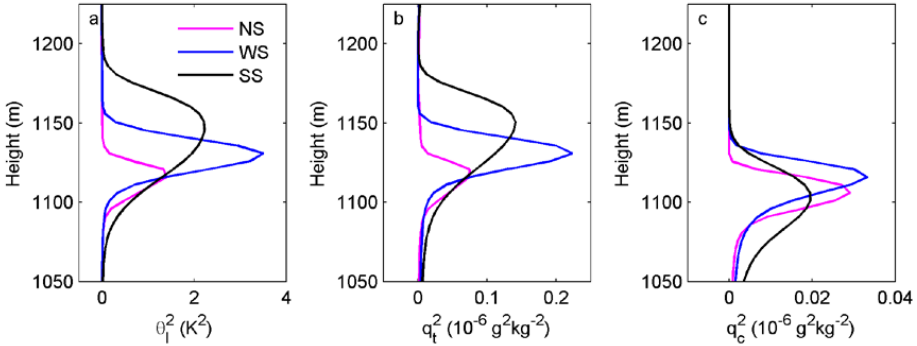

Fig. 5. Profiles of scalar variances within the inversion. **(a)** $\overline{\theta_l'^2}$; **(b)** $\overline{q_t'^2}$; and **(c)** $\overline{q_c'^2}$.

ACPD
12, 4941–4977, 2012

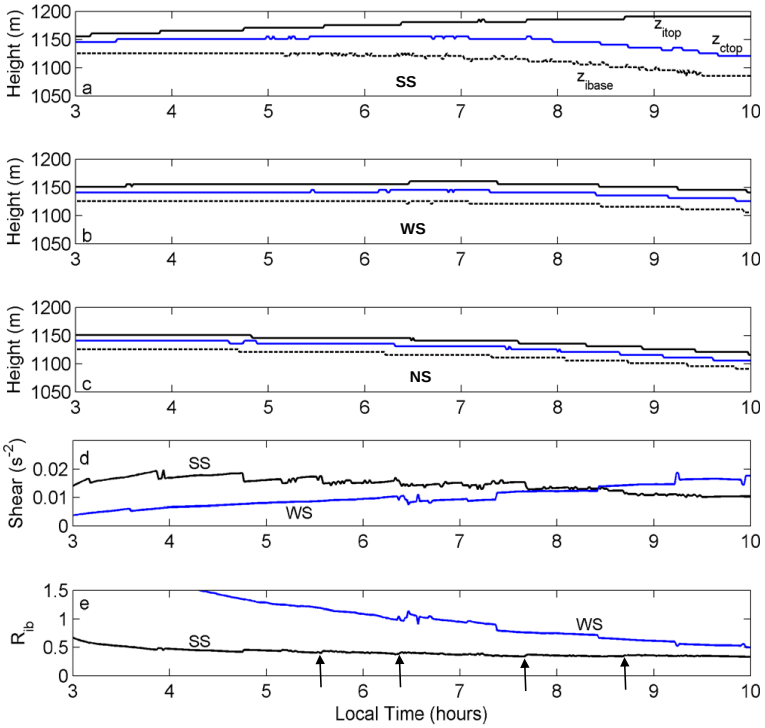

Fig. 6. Temporal evolutions of the inversion layer characteristics. **(a–c)** Evolution of the inversion top z_{itop} (solid black curve), inversion base z_{ibase} (dashed black) and cloud-top heights z_{ctop} (blue); **(d)** the wind shear factor in the denominator of Eq. (1) with the black curve for SS and blue for WS; and **(e)** the bulk Richardson number Ri_b with the black for SS and blue for WS. The wind shear and Ri_b are ill-defined for SN. Arrows at the bottom point to small jumps in Ri_b for SS, which are associated with the corresponding increases in Δz_i and decrease in the shear exhibited in **(a)** and **(d)**.

ACPD
12, 4941–4977, 2012

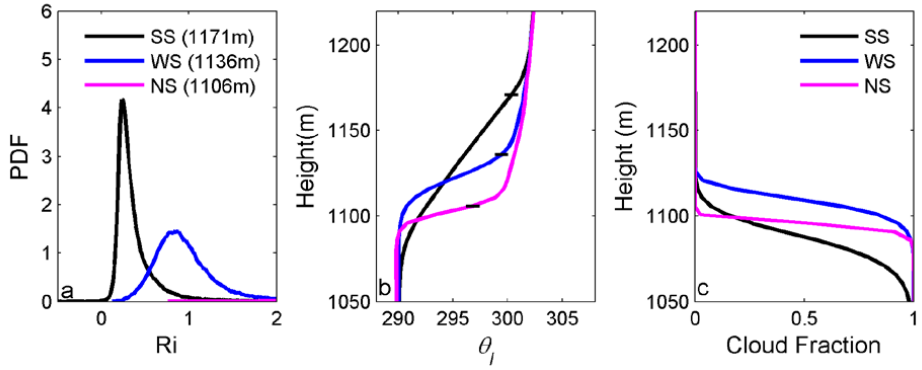

Fig. 7. Characteristics of the inversion layer. **(a)** PDF of the local gradient Richardson number (Ri); **(b)** $\bar{\theta}_l$ profile; and **(c)** cloud fraction profile. The levels at which the PDF(Ri) is derived are denoted by horizontal bars on the corresponding θ_l profiles. These levels are within the cloud-free sublayers as seen from the $\bar{\theta}_l$ and cloud fraction profiles.

ACPD
12, 4941–4977, 2012

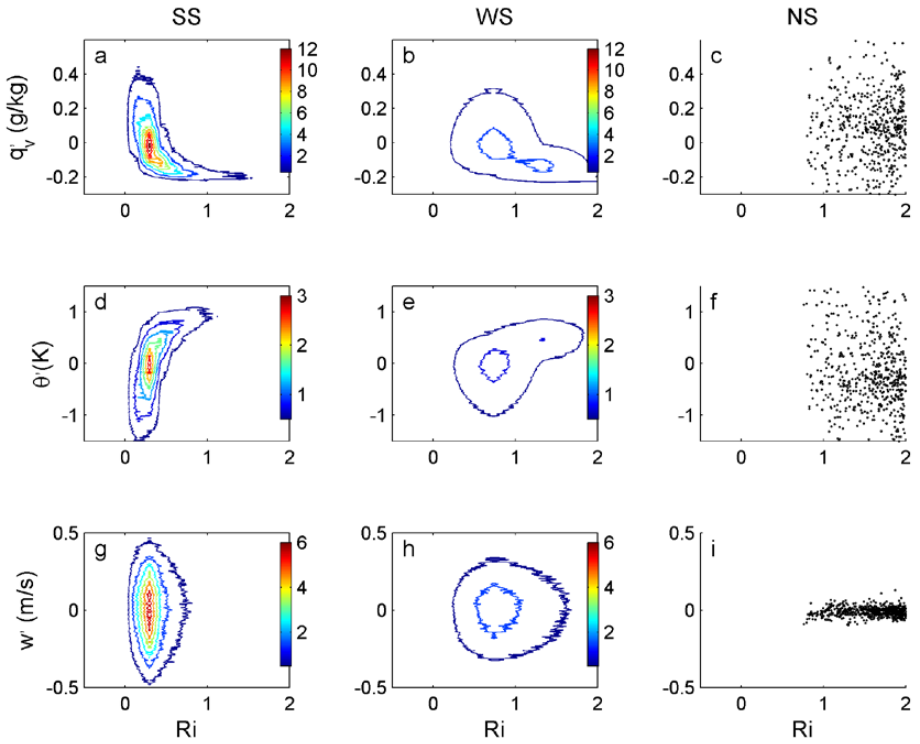

Fig. 8. Joint PDF of Ri with other variables (q_v, θ and w) in the cloud-free sublayer. The first column is for SS; the second WS and the third NS. The first row presents $Ri - q_v'$ joint PDF; the second $Ri - \theta'$; and the third $Ri - w'$. For the WS simulation (3rd column), only scattered plots are provided for the lower end of Ri.

ACPD
12, 4941–4977, 2012

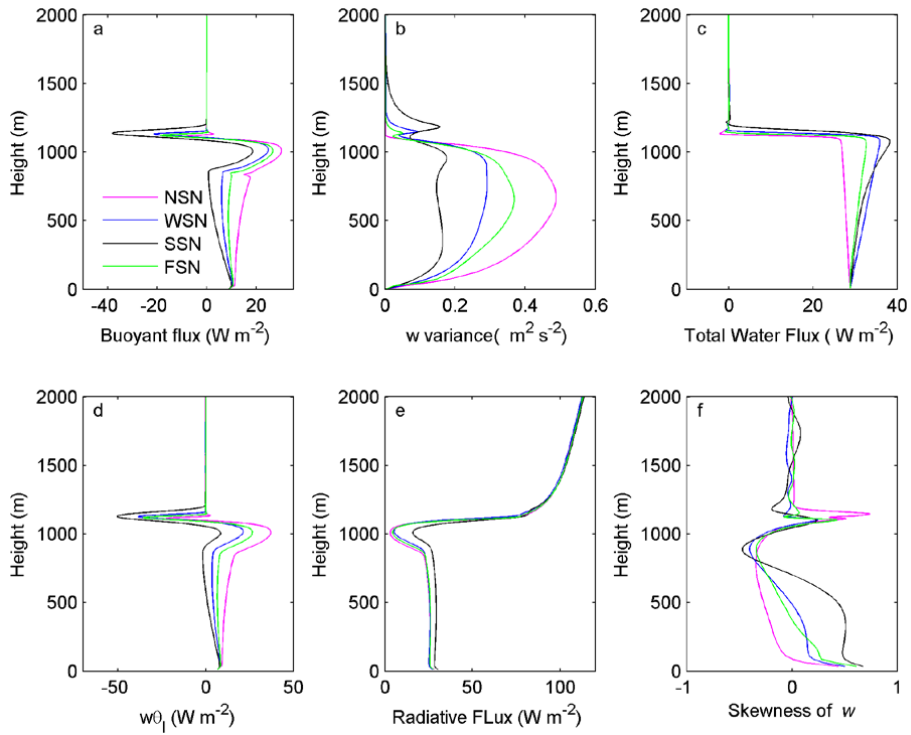

Fig. 9. Profiles of turbulence variables for four no-solar simulations. **(a)** $C_p\rho_0\overline{w'\theta'_v}$; **(b)** $\overline{w'^2}$; **(c)** $L\rho_0\overline{w'q'_t}$; **(d)** $C_p\rho_0\overline{w'\theta'_l}$; **(e)** Longwave radiative flux; and **(f)** skewness of w, defined by $\overline{w'^3}/\sigma_w^{3/2}$ where σ_w is the standard deviation of w.

ACPD
12, 4941–4977, 2012

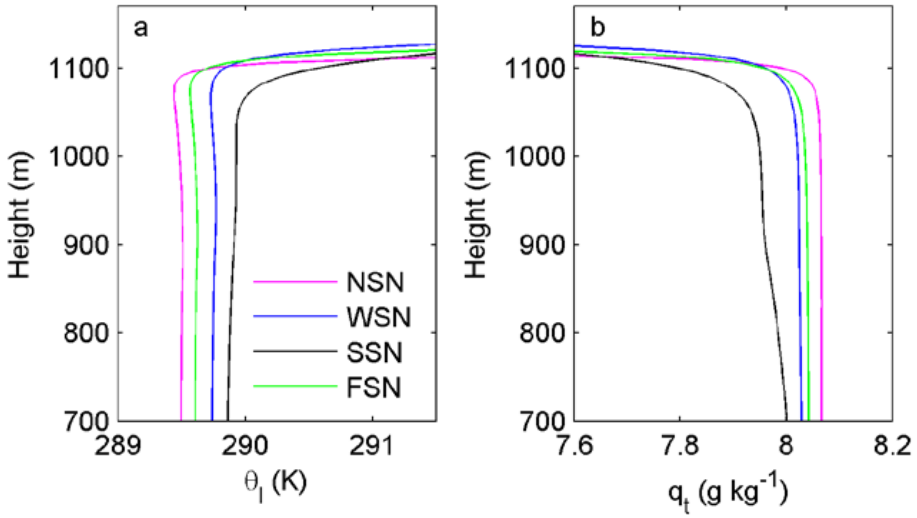

Fig. 10. Mean profiles for no-solar simulations. **(a)** $\bar{\theta}_l$; and **(b)** $\bar{q}_t$.

ACPD
12, 4941–4977, 2012

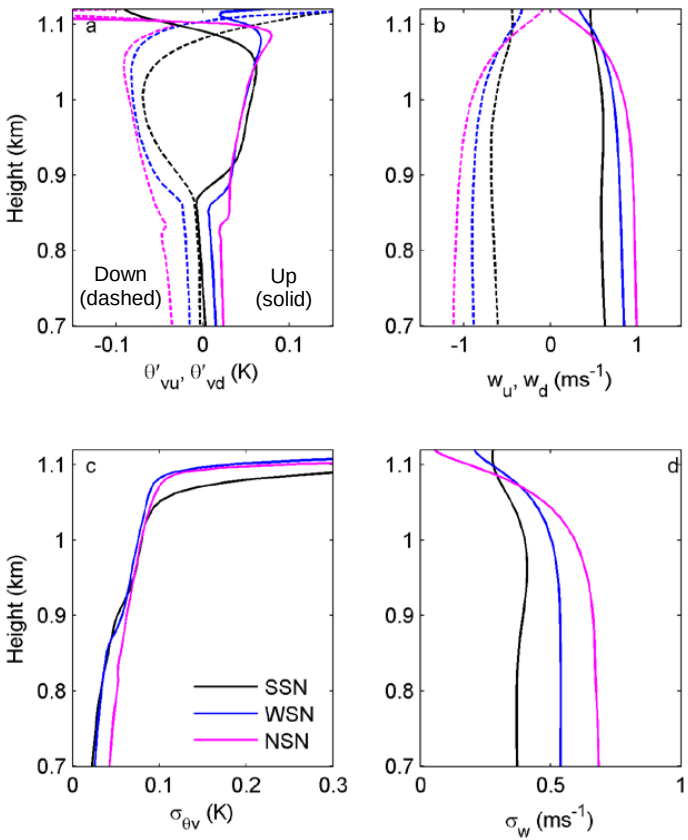

Fig. 11. Updraft-downdraft variables of convective circulation for no-solar simulations. **(a)** Averaged perturbations of buoyancy; **(b)** averaged updraft and downdraft velocity; **(c)** $\sigma_{\theta v}$; and **(d)** σ_w.

ACPD
12, 4941–4977, 2012